



# Minimum number of scans for collagen fibre direction estimation using Magic Angle Directional Imaging (MADI) with a priori information

Harry Lanz<sup>\*</sup>, Mihailo Ristic, Karyn E. Chappell, John V.M. McGinley

Mechanical Engineering Department, Imperial College London, London, UK

## ARTICLE INFO

### Keywords:

Collagen  
Magic angle  
Magnetic resonance imaging  
Tractography  
Soft registration

## ABSTRACT

Tissues such as tendons, ligaments, articular cartilage, and menisci contain significant amounts of organised collagen which gives rise to the Magic Angle effect during magnetic resonance imaging (MRI). The MR intensity response of these tissues is dependent on the angle between the main field,  $B_0$ , and the direction of the collagen fibres. Our previous work showed that by acquiring scans at as few as 7–9 different field orientations, depending on signal to noise ratio (SNR), the tissue microstructure can be deduced from the intensity variations across the set of scans. Previously our Magic Angle Directional Imaging (MADI) technique used rigid registration and manual final alignment, and did not assume any knowledge of the target anatomy being scanned. In the present work, fully automatic soft registration is incorporated into the MADI workflow and a priori knowledge of the target anatomy is used to reduce the required number of scans. Simulation studies were performed to assess how many scans are theoretically necessary. These findings were then applied to MRI data from a caprine knee specimen. Simulations suggested that using 3 scans might be sufficient, but in practice 4 scans were necessary to achieve high accuracy. 5 scans only offered marginal gains over 4 scans. A 15 scan dataset was used as a gold standard for quantitative voxel-to-voxel comparison of computed fibre directions, qualitative comparison of collagen tractography plots are also presented. The results are also encouraging at low SNR values, showing robustness of the method and applicability at low field.

## 1. Introduction

Magnetic Resonance Imaging (MRI) is routinely used for diagnostic imaging of various parts of the body because it offers unrivalled soft tissue contrast and it is safe, owing to the absence of harmful ionising radiation. However, conventional MRI does not provide sufficient information for accurate diagnostics of tissues containing large amounts of collagen, such as ligaments, tendons, articular cartilage, and the meniscus [1–4]. Particularly hard to diagnose are injuries such as partial ligament tears, for which surgical techniques such as arthroscopy remain the diagnostic gold standard, although they are normally undertaken only as therapy [1,5,6].

In these tissues the large collagen molecules are organised in fibre structures, and the MRI signal is produced by the hydrogen nuclei of the water molecules bound to collagen. Here, the major signal decay mechanism is the unaveraged dipolar coupling, resulting in extremely short relaxation time  $T_2$  and consequently a very low MRI signal. Such tissues normally appear very dark or even black, and any bright regions might be a sign of disease or injury, but they could also be caused by the well-known Magic Angle (MA) effect. Analysis of dipolar interactions leads to a simple formula showing that these interactions are minimised

when the angle between the collagen fibres and the main magnetic field  $B_0$  is  $\theta = 54.7^\circ$ , the Magic Angle. Therefore, for collagen molecules oriented at this angle, the time  $T_2$  can be significantly extended (from 1–2 ms to perhaps 20 ms) to result in a strong MRI signal.

The MA effect has long been considered as an unwanted source of imaging artifacts [7] that can be reduced using certain techniques. However, this effect can also be employed to provide valuable new information about the tissue microstructure. By analysing image intensities in scans obtained at various orientations to the main field,  $B_0$ , it is possible to estimate the collagen fibre orientation in a voxel and to obtain 3D tractography plots of the fibre structures. For example, Szevenyi et al. scanned a goat knee meniscus at 15 orientations to  $B_0$ , and used correlation between the measured intensities and those predicted using theoretical relationships for a large set of predefined candidate directions [8]. Seidel et al. performed a similar study on a human iliotibial tract sample [9]. They performed 35 scans constrained to two planes and computed the fibre directions by analysing the maxima of the intensity vectors versus simulated fibre directions.

In view of the practical difficulties of performing lengthy scanning of humans, our previous work [10,11] was aimed at minimising the

<sup>\*</sup> Corresponding author.

E-mail address: [harry.lanz15@imperial.ac.uk](mailto:harry.lanz15@imperial.ac.uk) (H. Lanz).

number of scan directions required for accurate estimation of fibre directions, for the case when no a priori knowledge about the expected fibre directions is available. We proposed the MAgic Angle Directional Imaging (MADI) method as an extension of the methodology of Szevenyi et al. [8], by choosing the scanning orientations evenly spread over the hemisphere, and by employing an optimisation step to maximise the accuracy of the computed fibre direction. We found that by doing this it is possible to use only 7 scan directions to robustly estimate fibre directions, even for images with relatively low signal-to-noise ratios (SNR).

The present work addresses the need to minimise the number of scans necessary for the MADI technique, improving on our previous work from [10] by taking a priori knowledge of target anatomy into account. Clinical application of the MADI technique is limited by data acquisition time and geometry requirements for the scans at various orientations. A single scan can take several minutes, and conventional MRI scanners are static and patients cannot be easily moved relative to them. Geometrical issues are addressed by our research group's development of a prototype rotatable scanner [12], yet it is still important to reduce data acquisition time by taking the fewest number of scans possible. This necessitates calculation of the optimal scanning orientations to use. The present work is therefore important to improve and assess the clinical feasibility of the MADI technique.

In this paper we set out to investigate how a priori information about the expected fibre directions may be employed to further reduce the required number of scanning orientations, whilst maintaining the accuracy of the technique. Simulation studies were performed on a virtual collagen fibre with known orientation in order to find theoretical optimal scanning orientations within a certain tolerance. MADI was then applied to real MRI data of a caprine knee specimen using 15 scanning orientations. MADI was then also applied to subsets of this 15 scan dataset, using scanning orientations found in the simulation studies, to assess whether only 3, 4, or 5 scans would be necessary.

In clinical practice, scout scans are normally used to capture the overall anatomy and plan the detailed scans. These can also be readily used by a medical specialist to define the expected healthy fibre directions in order to define the field orientations for the subsequent detailed scans. For example, in the case of ligaments, the expected fibre orientation would clearly be along the ligament to result in its maximum tensile strength, and local deviations from this could be a sign of injury or disease.

We have also updated the overall image processing pipeline to include soft registration. In our previous work we introduced registration based on fiducial markers as a method to align 3D images obtained at various directions of  $B_0$ , instead of relying on the measurements of the rotation angles that was employed by other researchers. However, MR images inevitably involve a certain amount of geometric distortion due to the linearity tolerances of the gradient field as well as the main field, which can make fiducial-based rigid registration insufficiently accurate in high-resolution images and demands manual fine adjustment, though often of no more than one or two voxels. Our aim was therefore to establish that soft registration could be adequately employed to fully automate this task while achieving accurate results.

## 2. Methods

### 2.1. Magic Angle Directional Imaging (MADI)

Fullerton and Rahal [13] found that at physiological hydration levels, 89% of the water in collagen rich tissues is 'orientationally restricted'. Dipole-dipole interactions between the proteins that make up collagen and the water molecules orient the water molecules transversely to the collagen fibre direction in a regular repeating structure. Due to this there are residual dipolar couplings oriented in the fibre direction, giving collagen rich tissues a very short T2 which yields low MR signal intensity. However, when the fibres are oriented at the

Magic Angle relative to  $B_0$ , the dipole interactions are overcome and the relaxation time of collagen rich tissues is increased, thus increasing the measured signal as shown in Fig. 1. Szevenyi and Bydder [8] modelled the resulting MR angle sensitivity of collagen fibres as:

$$I = A \cdot \exp(-B \cdot (3 \cos^2 \theta - 1)^2) \quad (1)$$

where  $I$  is the recorded intensity,  $A$  and  $B$  are constants, and  $\theta$  is the angle between the collagen fibre direction and  $B_0$ . Knowing this relationship, it is possible to deduce the orientation of collagen fibres from multiple scans of the same subject at different  $B_0$  orientations. Each  $B_0$  orientation, defined in the scanned subject's reference frame, is referred to as a scanning orientation.

Following our previous work [10,11], the overall MADI method may be summarised as follows:

1. Acquire  $N$  scans of the subject using  $N$  different  $B_0$  orientations.
2. Register the acquired  $N$  volume images.
3. Detect voxels with significant intensity variation as the likely collagen-containing voxels; on this basis segment the region of interest (ROI).
4. For a predefined set of candidate directions, use Eq. (1) to calculate theoretical intensities corresponding to  $N$  scans.
5. Estimate fibre direction for each voxel in ROI:
  - (a) Find the candidate direction in the set, which has the theoretical intensities with the highest correlation to the measured ones, and use it as the initial guess for the optimisation step.
  - (b) Use an optimisation process to compute the fibre direction that maximises the correlation between the theoretical and measured intensities.

The predefined candidate directions in step 4 were a bouquet of 400 directions uniformly distributed on a hemisphere, which had been previously shown to lead to robust initial guess for the subsequent simplex minimisation [10]. In the cases considered here, where a priori knowledge was available, this was reduced to a subset of 100 candidates, with a higher density near the assumed direction. However, the whole hemisphere was still spanned to avoid overfitting.

The optimisation step 5b was performed using the Nelder-Mead simplex algorithm to minimise:

$$C(\mathbf{x}) = \sum_{k=1}^N (I_k^M - I_k^C(\mathbf{x}))^2 \quad (2)$$

where  $C(\mathbf{x})$  is the cost as a function of the current computed fibre direction  $\mathbf{x}$  with  $N$  associated intensity values,  $I_k^M$  is the measured intensity (see Fig. 2) and  $I_k^C(\mathbf{x})$  is the computed theoretical intensity of a fibre with orientation  $\mathbf{x}$ .

### 2.2. Soft registration

The acquired volume images were first pre-aligned using rigid body registration based on fiducial markers, followed by soft registration which also allowed for any geometric distortions. The pre-alignment stage relies on 3 fiducial markers attached to the specimen, represented by 10 mm diameter water filled spheres (.43 Caliber Clear Paintballs 8000, Rap4 UK). Following the methodology of de Oliveira et al. [14] and Brujic et al. [10], these spheres were located in the MR images using the template matching technique and the Fourier filtering method [15]. This method was found to give a localisation accuracy of <0.3 voxels by Franco et al. [16]. Since the markers were arranged in an irregular triangle, each vertex was uniquely defined by which two side lengths of the triangle associated with it, allowing each marker to be unambiguously identified in a given 3D image. Rigid body registration was therefore performed as the translation and the rotation about the image centre of mass and to align the markers.

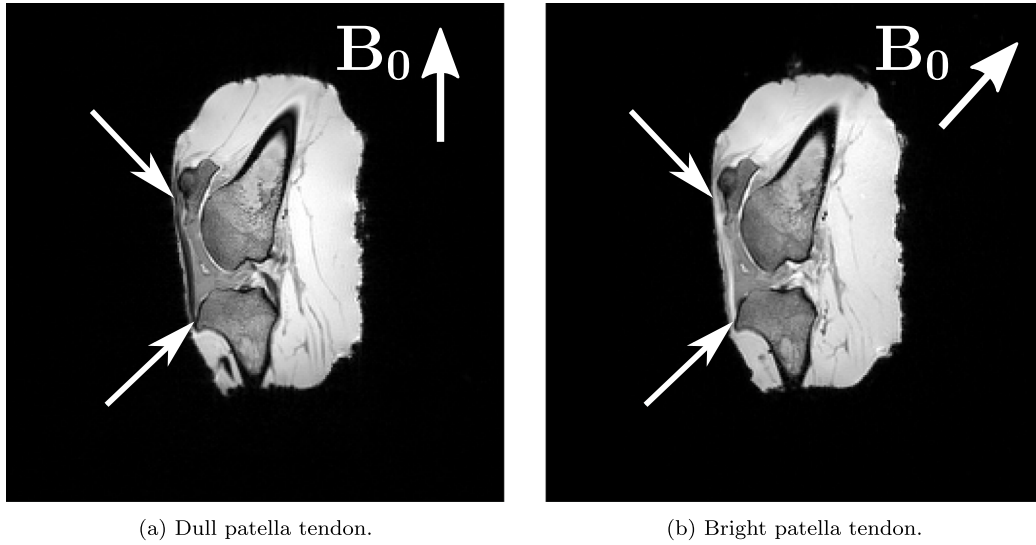


Fig. 1. Sample images of a caprine knee specimen obtained at different orientations to  $B_0$ . The attachment points of the patella tendon are shown by the white arrows. The Magic Angle effect is illustrated here as the patella tendon is dark in 1(a) yet much brighter in 1(b) as the main field was at approximately  $55^\circ$  to the collagen fibres in the tendon.

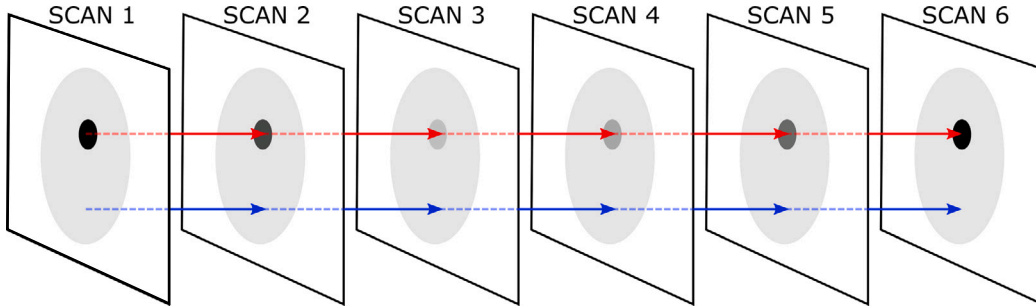


Fig. 2. An example set of six scans with different scanning orientations that have been registered. The dark inner area is representative of collagen and hence shows variable intensity. The red and blue lines show corresponding voxels in collagen rich and non-collagen rich regions respectively. (For interpretation of the references to colour in this figure legend, the reader is referred to the web version of this article.)

Soft registration was then performed by optimising a B-spline transform from the fixed to the moving image, and then assigning the interpolated values in the moving image to the corresponding voxels in the fixed image [17]. The parameterisation of the B-spline transform [17,18] was:

$$T_{c_k}(\mathbf{x}) = \mathbf{x} + \sum_{\mathbf{x}_k \in N_{\mathbf{x}}} c_k \beta^3 \left( \frac{\mathbf{x} - \mathbf{x}_k}{\sigma} \right) \quad (3)$$

where  $\mathbf{x}$  is the 3D coordinate being transformed,  $\mathbf{x}_k$  are the control points,  $N_{\mathbf{x}}$  is the set of all the control points within the compact support at  $\mathbf{x}$ ,  $c_k$  are the B-spline coefficient vectors,  $\sigma$  are the B-spline control point spacings [17], and  $\beta^3(\mathbf{x})$  is the cubic multidimensional B-spline polynomial [19]. The coefficient vectors  $c_k$  are the optimisation parameters and not  $\mathbf{x}_k$ . Changes to  $c_k$  affect the position of the control points and hence are used to optimise the transform rather than move  $\mathbf{x}_k$  directly.

The images obtained experimentally in this work were  $256 \times 256 \times 208$  (1 mm voxel size in each dimension) and the collagen structures of interest existed on length scales of  $\mathcal{O}(10^0)$  and  $\mathcal{O}(10^1)$  mm. Based on this, the control point spacing  $\sigma$  was set to 16 voxels (16 mm) in each direction allowing sufficiently fine control over the B-spline transforms without the need for heavy regularisation. Bending energy was used to penalise excessive curvature of the B-splines based on their second spatial derivatives [17], however, a low weight of 1 was assigned to this regularisation term, as spurious bending mainly occurs in large homogeneous regions due to lack of information, which was not an issue for our ROI.

The metric employed to quantify registration accuracy was the Mutual Information (MI) [20–22], defined by Thévenaz and Unser [23] as:

$$MI(\mu; I_F; I_M) = \sum_{m \in L_M} \sum_{f \in L_F} p(f, m; \mu) \cdot \log_2 \left( \frac{p(f, m; \mu)}{p_F(f) \cdot p_M(m; \mu)} \right) \quad (4)$$

where  $\mu$  are the transform parameters,  $I_F$  is the fixed image,  $I_M$  is the moving image,  $L_F$  and  $L_M$  are regularly spaced intensity bin centres for the fixed and moving images,  $p$  is the discrete joint probability,  $p_F$  and  $p_M$  are the marginal discrete probabilities of the fixed and moving images — obtained by summing  $p$  over  $M$  and  $F$  respectively [17]. Histogram bin widths were chosen based on the dynamic range of the images. The images in this work had fairly low dynamic range, the maximum voxel intensity was  $<400$ , therefore 32 histogram bins were used. MI is suitable for registration of multi modal images [17] as using MI helps to align features despite potential intensity differences, rather than simply matching intensities. Our data was single mode, but the angle-sensitivity of collagen rich tissues meant that certain structures showed significant intensity changes, necessitating a transform metric that was robust to intensity variations.

The B-spline transformation in Eq. (3) was optimised in terms of parameters  $\mu = c_k$ , based on the metric MI. The adaptive stochastic gradient descent method [24] was employed to optimise over a maximum of 1000 iterations. Once the transformation was optimised, the registered image was reconstructed from the moving image by transforming a voxel coordinate from the fixed to the moving image,

in which the intensity at this coordinate was obtained using cubic B-spline interpolation. This intensity was then recorded in a reconstructed image, at the original fixed image voxel coordinate.

When registering multiple scans, one of the 3D images was designated the fixed image and all other images were registered to it. Registration was further improved by applying a binary mask to the fixed image in order to exclude from the scope of the registration the noisy air surrounding the sample. The mask was produced by applying a 3D Gaussian blur with a kernel size of 61 and  $\sigma = 10$  to the fixed image. A threshold value based on the noise in the air then turned the blurred image into a 3D Boolean mask which included the specimen and a few layers of air around it for registration, whilst excluding the majority of the empty space.

Both the rigid and the soft registration steps were implemented using the *elastix* toolbox [17] as the functionality offered was sufficient for our needs.

### 2.3. Simulation studies

Assuming perfect registration, simulation studies involving a single collagen-rich voxel were performed to assess the overall performance for different numbers of scans  $N = 3, 4, 5$ , at angles  $\theta_{1...N}$  in the range  $15^\circ$ – $85^\circ$  in  $1^\circ$  increments. Eq. (1) was used to simulate MR image intensity in the voxel with added noise, and the fibre direction was then estimated using the MADI technique described above. The error angle between the computed fibre direction and the ground truth was recorded and stored in an  $N$ -dimensional matrix. The ground truth collagen orientation was along the  $Z$  axis. Intensity values for different angles  $\theta$  were with constants  $A = 300$  and  $B = 1$  in Eq. (1). The final intensity value was taken from a normal distribution with  $\mu = I$  from Eq. (1), and  $\sigma = 20$  which was chosen to approximate the standard deviation seen in the real MR data from Section 2.4. Absolute values were taken to avoid negative intensities in low signal regions far from the Magic Angle.

### 2.4. MRI data acquisition

We have previously conducted extensive experiments [10,11] to obtain reference MRI scan data of a caprine knee specimen. The specimen was mounted inside a plastic sphere with marking which allowed the sample to be rotated in order to achieve known orientations relative to  $B_0$ . Scans were obtained at 15 different orientations which were chosen to be equally distributed on a hemisphere. A 12-channel head coil was the signal receiver. Volume scans were performed using a 3T hospital scanner (Magnetom Verio, Siemens, Erlangen, Germany), using a 3D T1 FLASH (Fast Low Angle SHot) sequence: TR 13 ms, TE 4.9 ms. The image resolution was  $1 \text{ mm}^3$  voxels with an image volume of  $256 \times 256 \times 208$  voxels. This data allowed for comparison of the updated MADI technique to previous work and also served as a gold standard reference for subset studies in Section 3.2.

### 2.5. Studies using MRI data

The reference dataset consisting of all 15 scans was first used with the MADI method described above with no assumed a priori knowledge about the collagen orientation. In this way we generated reference tractography results for the patella tendon, which was subsequently used as the basis for evaluation of results involving reduced number of scans and added image noise. Justification for this approach was our previous work [10], which has shown that accurate results are obtained using 7 scans in the case when no a priori knowledge is available, therefore we assumed that using 15 scans with high SNR ( $\text{SNR} > 50$ ) is more than adequate to provide a gold standard of method performance.

In subsequent studies we used subsets of  $N = 3, 4, 5$  from the full set of 15 reference scans, with orientations that were closest to the desired ones. Therefore this assumed that the orientation could be controlled

**Table 1**

The average angle the computed fibres in the patella tendon made with  $B_0$  for each scan.

| Scan              | 1   | 2    | 3    | 4    | 5    | 6    | 7    | 8    | 9    | 10–15 |
|-------------------|-----|------|------|------|------|------|------|------|------|-------|
| Mean $\theta$ [°] | 9.3 | 34.0 | 24.6 | 29.0 | 35.4 | 62.0 | 68.8 | 61.8 | 56.5 | 80–85 |

with an accuracy of about  $\pm 7^\circ$ , which is considered reasonable for practical situations.

The effect of noise was analysed by adding Rician noise to the images [25] corresponding to certain SNRs. SNR was calculated as:

$$\text{SNR} = \frac{|Signal|}{StDev(Noise)} \quad (5)$$

where  $|Signal|$  is the mean signal, calculated by taking the mean of all intensities in a dataset within a mask of the specimen, and  $StDev(Noise)$  is the standard deviation of the noise in the air around the specimen. The mask used for the mean signal calculation was a slimmed version of the registration mask, so not to include the air surrounding the specimen, while an expanded version of the same mask was used to calculate the standard deviation of noise in the air and to exclude any signal from the specimen.

In all studies, the collagen-rich regions of the images were segmented via two interactive steps. A cuboid ROI was first selected interactively on the fixed image, and then applied to the subsequent registered images. Standard deviation of the intensity was calculated across all corresponding voxels in the ROI to produce a standard deviation image, where bright, high standard deviation voxels were likely to contain collagen. The standard deviation was normalised by the maximum value and the user then iteratively set a threshold,  $[0..1]$ , to isolate voxels with significant standard deviation. The user was presented with a 3D plot of all the voxels in the ROI above the threshold. This visualisation ensured the collagen structure of interest was suitably captured before fibre direction computation. Discretion was required to avoid inclusion of too many non-collagen containing voxels resulting from artefacts, such as the partial volume effect or registration errors. Once chosen, the user then selected a contiguous collection of voxels that represented the collagen structure of interest to be segmented.

To quantify how accurate a given test configuration was, the angular separation (deviation) was recorded for each set of corresponding voxels between each  $N = 3, 4, 5$  subset and the  $N = 15$  scan dataset. The deviations were binned into histograms with bin sizes of  $5^\circ$ – $25^\circ$  and the proportion of angles in each bin was recorded. This necessitated that the same segmentation label was used for  $N = 15$  and its subsets.

## 3. Results

The MADI technique was applied to the  $N = 15$  scan dataset, the scanning orientations used were chosen to allow for any collagen fibre direction to be estimated and to serve as a gold standard for subsequent comparisons using subsets of this dataset. The patella tendon shown in Fig. 1 was segmented and represented by 2080 voxels, or  $2080 \times 15$  corresponding voxels across all scans, yielding 2080 estimated fibre directions. Fig. 3 shows the measured intensity vs the angle to  $B_0$  for each computed fibre direction for each scan. Each computed fibre direction relates to 15 data points in Fig. 3, where the straightness of the patella tendon is illustrated by the data points for each scan being grouped together. The theoretical intensity variation from Eq. (1) is shown to fit well with the measured data, particularly around the Magic Angle.

Table 1 contains the mean of all 2080 fibre directions for each scan relative to  $B_0$  for that scan, since the patella tendon is relatively straight, these means were used to quantify the macroscopic tendon orientation relative to  $B_0$ .

Fig. 3 shows that the intensity response of the collagen is well sampled over the full spectrum of angles when using  $N = 15$  even



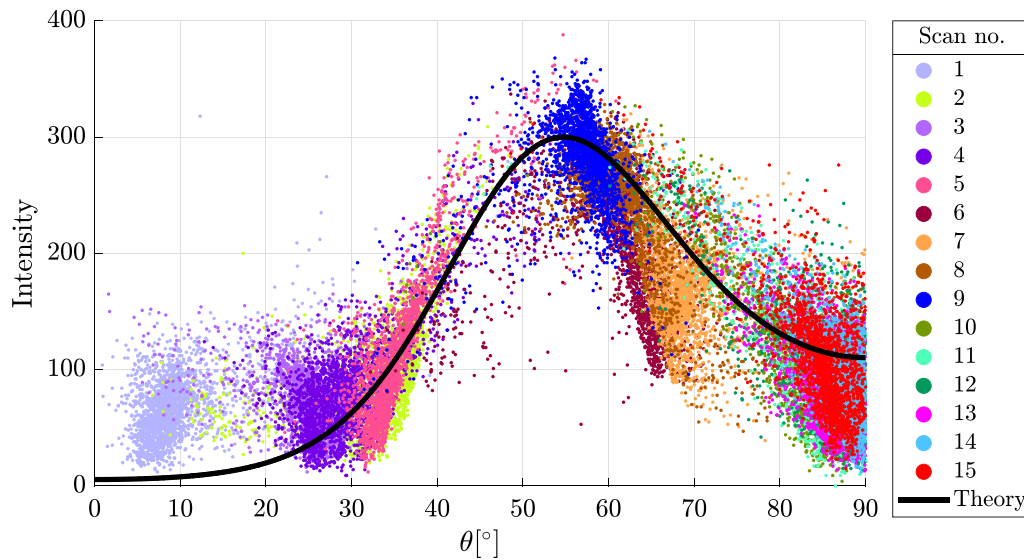


**Fig. 3.** Intensity vs.  $\theta$  for each computed fibre direction in the ROI across all  $N = 15$  scans, points in each scan indicated by a distinct colour. (For interpretation of the references to colour in this figure legend, the reader is referred to the web version of this article.)

spaced scanning orientations. We hypothesised that a set of  $N = 3$  scanning orientations would be sufficient to estimate fibre directions if the peak intensity response was sampled at the Magic Angle as well as one data point either side. To identify suitable choices of scanning orientations we performed simulation studies on a single voxel with known collagen fibre direction along the  $Z$  axis. With  $N = 3, 4, 5$  the deviation of the computed fibre direction from ground truth was recorded in an  $N$  dimensional matrix.

### 3.1. Simulation study results

Fig. 4 a–f shows the deviation surfaces formed by the recorded deviations with  $\theta_1$  and  $\theta_2$  in the range  $15^\circ$ – $85^\circ$  and the remaining angles at chosen static values in order to visualise the deviations as a 3D surface. The blue regions highlight areas with deviation of less than  $10^\circ$ . The results show symmetry along the  $\theta_1 : \theta_2$  diagonal as expected. Fig. 4a shows a low deviation region at  $[\theta_1, \theta_2, \theta_3] = [40^\circ, 70^\circ, 55^\circ]$  in agreement with our hypothesis. Fig. 4d shows the results when  $\theta_3 = 50^\circ$  showing that the method is robust even if the intensity peak at the Magic Angle is not perfectly captured.

Fig. 4b shows a similar deviation surface with  $\theta_1$  and  $\theta_2$  in the range  $15^\circ$ – $85^\circ$  and  $\theta_3 = 55^\circ$  and  $\theta_4 = 70^\circ$ . The low deviation regions have expanded suggesting an increased robustness of using 4 scanning orientations relative to 3.  $\theta_4$  was chosen to visualise the data in Fig. 4b from the region of low deviation in Fig. 4a. Again Fig. 4e shows the results with  $\theta_3 = 50^\circ$  illustrating robustness across a range of  $\theta_3$ .

Fig. 4c shows a deviation surface with  $\theta_1$  and  $\theta_2$  in the range  $15^\circ$ – $85^\circ$  and  $\theta_3 = 55^\circ$ ,  $\theta_4 = 40^\circ$  and  $\theta_5 = 70^\circ$  where the entire surface is a low deviation region. Since the static angles  $\theta_3, \theta_4, \theta_5$  are already good low deviation choices for scanning orientations, any additional choice of angles  $\theta_1$  and  $\theta_2$  also yield low deviation. The central region of Fig. 4c near  $\theta_1 = \theta_2 = \theta_3$  shows the highest deviation as the additional scans are redundant. Fig. 4f shows the surface with  $\theta_3 = 50^\circ$ , also an entirely low deviation surface.

The results from the simulation studies and Table 1 were used to select the  $N = 3, 4, 5$  subsets to test the MADI technique with fewer scans. We chose scanning orientations in the low deviation regions found in the simulation studies. The patella tendon was relatively straight hence the means in Table 1 are representative of the tendon's angle to  $B_0$  for a particular scan. The chosen subsets and their mean orientations to  $B_0$  are given in Table 2.

**Table 2**

Scans chosen for  $N = 3, 4, 5$  subsets and the mean angle of the patella tendon relative to  $B_0$  for each scan.

| N | Scans  |
|---|--|
| 3 | 5 ( $34.5^\circ$ ), 7 ( $68.8^\circ$ ), 9 ( $56.5^\circ$ ) |
| 4 | 4 ( $29.0^\circ$ ), 5, 7, 9                                |
| 5 | 4, 5, 7, 9, 13 ( $80.0^\circ$ )                            |

### 3.2. MRI data subset results

When imaging a healthy tendon, there is a high degree of fibre alignment which is what the a priori knowledge is based on. Damaged areas can be detected with the MADI technique as shown by Chappell et al. [11] in our previous work. Damaged/ruptured tendons were identified from tractography and fibre direction data as areas with discontinuous or misaligned fibres. The damage in these regions was subsequently confirmed via dissection. In our previous work, 9 scans were used to achieve these results hence any fibre direction would be very likely to be resolvable. When using only 4 scans and a priori knowledge, we would expect that a damaged area will show misaligned/discontinuous fibres or the fibre directions will not converge in this region due to being too far from the a priori assumption; thus damaged areas will still be identifiable. However, the scope of the present work focuses on assessing the accuracy of fibre estimation using minimal numbers of scans, hence we chose to study a healthy caprine patella tendon since it has fairly simple geometry and highly aligned fibres.

Fig. 5 shows the fibre directions assigned to each voxel for  $N = 3$ . This vector field-like representation of the fibres allows for a detailed view of the local fibre directions within the tendon. Each fibre direction estimation is denoted with a coloured line pointing from a voxel location, marked as a black dot. The RGB colour of the line is determined by the axes it aligns with, alignment along the  $x$  axis would only have a red component, and only blue and only green for the  $y$  and  $z$  axes respectively. For directions not perfectly aligned with an axes the RGB values are interpolated. Fig. 5 shows a high degree of fibre alignment as the fibres can be seen to flow into each other from voxel to voxel and almost all of them are marked green or a shade of green. If damage were present this visualisation technique would be useful for a detailed voxel level view of the region. However, to better understand the tendon structure in 3D and in the context of other anatomy, tractography was generated.

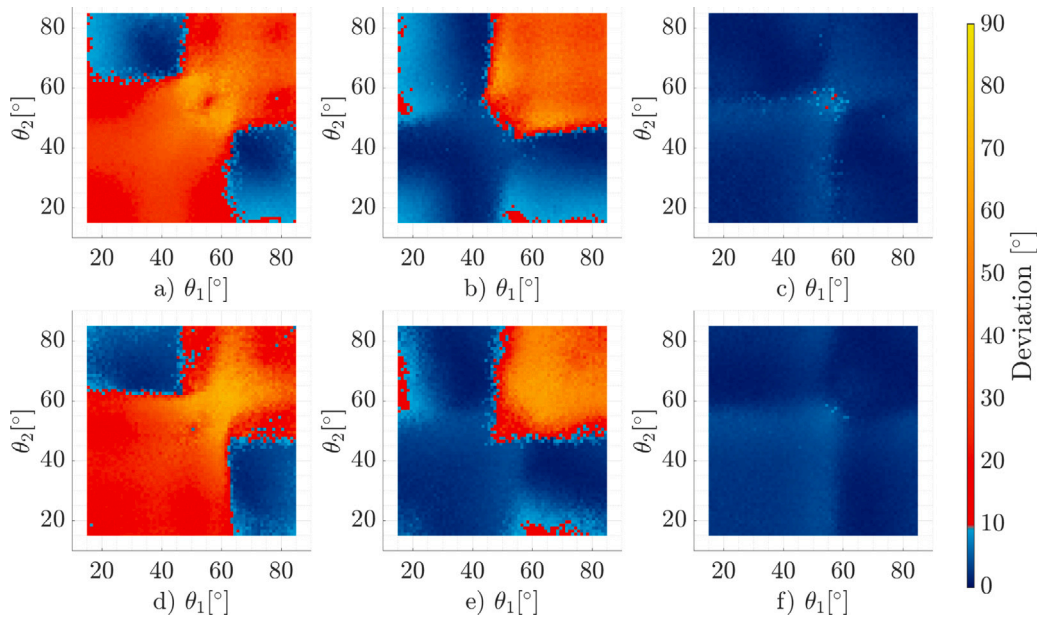


**Fig. 4.** Deviation surfaces from single voxel simulation studies. The top row has  $\theta_3 = 55^\circ$  and the bottom row has  $\theta_3 = 50^\circ$ . (a) and (d) show the deviation surface using 3 scanning orientations, (b) and (e) with 4 scanning orientations with  $\theta_4 = 70^\circ$ , and (c) and (f) with 5 scanning orientations with  $\theta_4 = 70^\circ$  and with  $\theta_4 = 40^\circ$ . (For interpretation of the references to colour in this figure legend, the reader is referred to the web version of this article.)

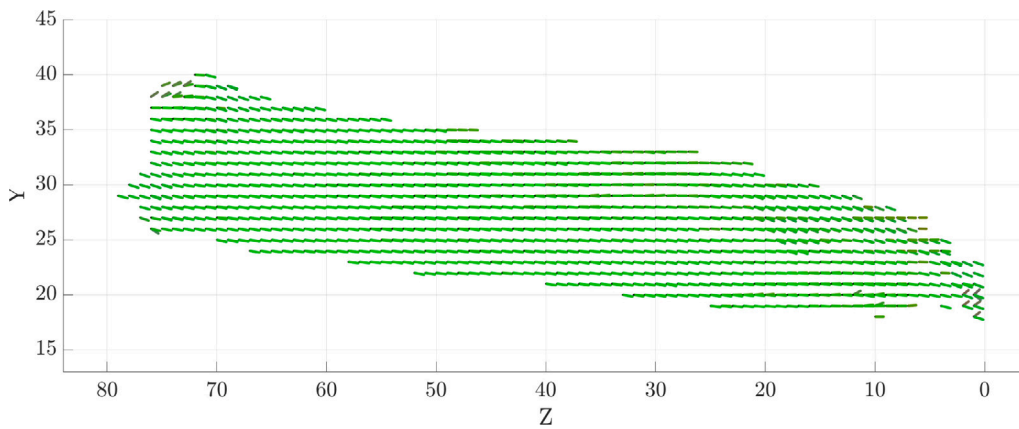


**Fig. 5.** Fibre directions assigned to each set of corresponding voxels for  $N = 3$ . (For interpretation of the references to colour in this figure legend, the reader is referred to the web version of this article.)

Tractography results for  $N = 3$ ,  $N = 4$  and  $N = 15$  scans are shown in Fig. 6, using the same colouring scheme as in Fig. 5. Tractography visualisation of the tendons in Fig. 6 was produced using Slicer [26] with the diffusion tensor imaging extension [27], by converting our fibre direction estimations into synthetic diffusion tensors. The bones were hand-segmented from the images to provide context to the tendon. Qualitatively, the quality of the tractography improves noticeably from  $N = 3$  to  $N = 4$ , with  $N = 15$  displaying the gold standard.  $N = 4$  is of comparable quality to  $N = 15$ .  $N = 5$  tractography is not shown here but was almost identical to  $N = 4$ . The tractography results show highly aligned fibres along the tendon indicating similarly to Fig. 5. We used the same segmentation label for  $N = 15$  on all the subsets in order to allow for direct voxel to voxel comparison between the gold standard and the  $N = 3, 4, 5$  studies.

To quantify how accurate a given test configuration was, the angular separation (deviation) was recorded for each set of corresponding voxels between each  $N = 3, 4, 5$  subset and the  $N = 15$  scan dataset. The deviations were binned into histograms with bin sizes of  $5^\circ$ – $25^\circ$  and the proportion of angles in each bin was recorded.

Figs. 7, 8, and 9 show the accuracy of the  $N = 3, 4, 5$  scan subsets at different SNRs using voxel to voxel comparison to the gold standard.

$N = 3$  yields a large spread of deviations with only 35% and 50% of computed directions being within  $5^\circ$  and  $10^\circ$  respectively. The improvement when using  $N = 4$  is evident as the proportion angles within  $5^\circ$  and  $10^\circ$  of the gold standard increases to 70% and 95%. The improvement from  $N = 4$  to  $N = 5$  is less pronounced with less than a 5% increase for angles within  $5^\circ$  and less than 2% for angles within  $10^\circ$  of the gold standard. Figs. 7–9 all show a consistent accuracy until approximately an SNR of 25 at which point there is a steep decline as the data becomes too corrupted to estimate fibre directions.

Fig. 10 shows the alignment index of the patella tendon for  $N = 3$ ,  $N = 4$ , and  $N = 15$ . We previously used alignment index as a measure of anisotropy of the computed fibre directions which we correlated with tendon maturity [11]. The alignment index was calculated by

$$AI = \frac{n_M - n_{rnd}}{n_{total} - n_{rnd}} \quad \text{if } n_m > n_{rnd} \quad \text{else} \quad AI = 0 \quad (6)$$

where  $n_{total}$  was the total number of fibre directions computed,  $n_M$  was the number of fibre directions within  $20^\circ$  of a specified orientation, and  $n_{rnd}$  is the number of random directions within  $20^\circ$  of the specified orientation out of  $n_{total}$  random orientations. In our previous work we found that more mature tendons had a higher alignment index than

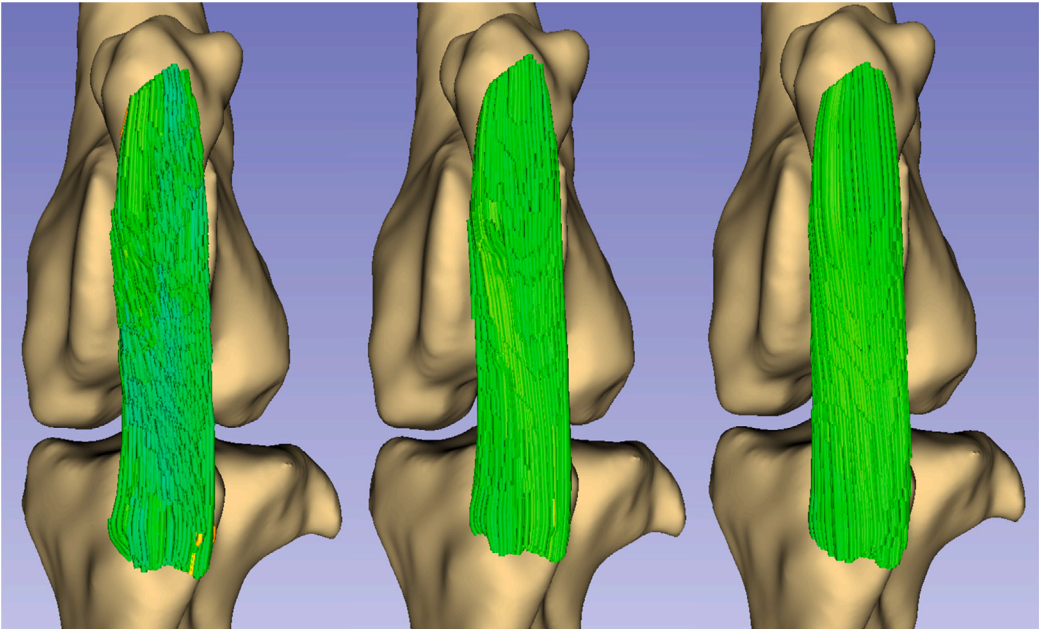


**Fig. 6.** Application of the Magic Angle Directional Imaging technique to render the patella tendon of a caprine knee specimen using tractography. Left to right shows the results from 3, 4 and 15 scans respectively, where 15 scans is the gold standard for comparison. The tract colour is a function of its local orientation. Greener regions align more with the  $y$  axis.

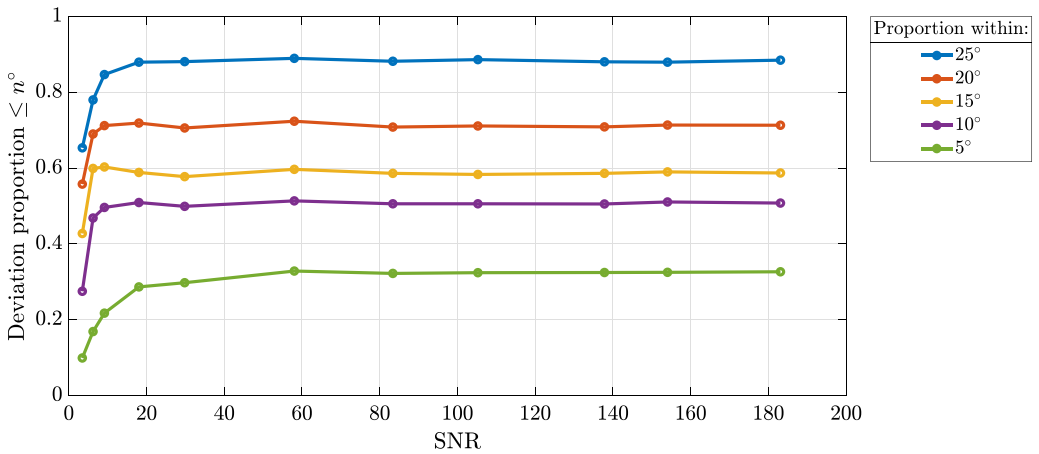


**Fig. 7.** Accuracy and SNR robustness of 3 scan subset when compared to 15 scan gold standard.

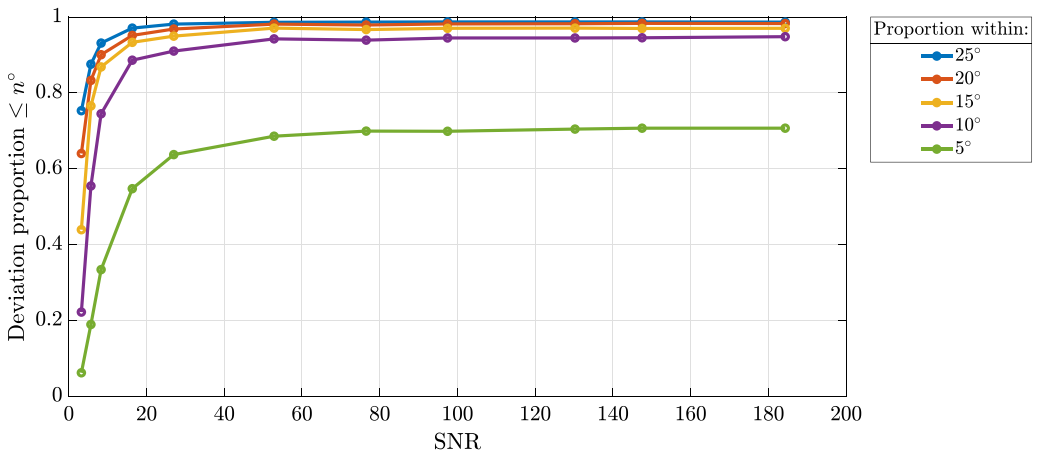


**Fig. 8.** Accuracy and SNR robustness of 4 scan subset when compared to 15 scan gold standard.

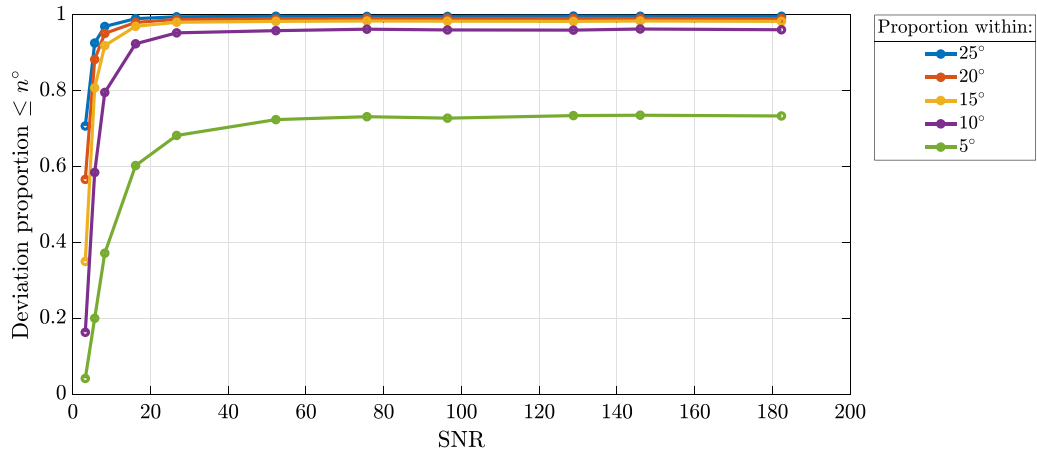


Fig. 9. Accuracy and SNR robustness of 5 scan subset when compared to 15 scan gold standard.

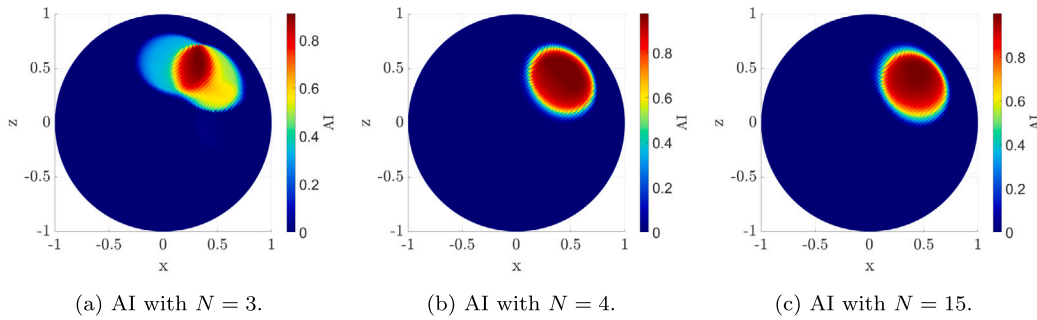


Fig. 10. The alignment indices for 10(a):  $N = 3$ , 10(b):  $N = 4$ , 10(c):  $N = 15$  plotted on a unit sphere.

younger tendons provided the tendon was healthy. This result is again shown in the present work in Fig. 10(c) for the  $N = 15$  gold standard. Fig. 10(a) shows the  $N = 3$  alignment index which has two obvious regions of alignment shown by the dual lobes. Fig. 10(b) shows the alignment index for  $N = 4$  which is very similar to the  $N = 15$  result.

#### 4. Discussion

Previously we have shown that 7–9 scans are sufficient to accurately estimate any collagen fibre direction, with no a priori knowledge of their orientations, depending on SNR. However, for a given fibre direction, some scans are likely to be redundant due to sampling the same domain of the intensity response as each other. This effect is evident in Fig. 3 where the data from multiple scans overlaps. In the present work we have shown that with some a priori knowledge of the target anatomy this can be avoided and theoretically 3 scans can be used, but in practice 4 scans are necessary to yield sufficiently accurate results. The voxel-to-voxel comparisons and alignment indices shown in Figs. 7–10 illustrate that  $N = 4$  can yield comparable results to the gold standard with some a priori knowledge. This is also evident qualitatively from the tractography in Fig. 6.

Using 3 scans gave somewhat reasonable results, yet with only 3 scans the potential for some directions to be under-constrained was higher. This is particularly evident in the difference between Figs. 10(a) and 10(b) where the addition of one more scanning orientation was sufficient to correct the alignment of a significant portion of the fibres. Our initial hypothesis was partly correct in that we did have success when sampling the peak intensity response plus one scan either side of it, but we found it necessary to add an additional scan to properly estimate the directions. Since we used data collected assuming no a priori knowledge of the target anatomy, the subsets of scanning orientations used were chosen as they were close enough on average

to what the simulation studies suggested. In future work further gains in accuracy could be made with precise control over the scanning orientations relative to target anatomy, perhaps increasing the viability of using only 3 scans, or further improving the 4 scan results.

With the eventual aim to apply the MADI technique using our prototype low field scanner [12], fewer scans for accurate results is of practical importance to reduce data acquisition time. A scout scan will likely be necessary to establish a priori knowledge of the target anatomy, and then the data acquisition will follow. The diminishing returns of increasing from  $N = 4$  to  $N = 5$  suggest that it would not be worthwhile to perform an additional scan unless the target anatomy was particularly complex. A curved tendon would in theory require extra scans to compute its fibre directions for the whole tendon as the relative scanning orientation would vary across the structure. In the present work this was not an issue as the patella tendon was relatively straight.

Since voxels are on the order of  $\mathcal{O}(10^{-1})$  to  $\mathcal{O}(10^0)$  mm<sup>3</sup> in size, fibres can be considered straight at this scale, hence the method is always valid for a single given voxel. On a more macroscopic scale such as a tendon, which generally have sizes on the order of  $\mathcal{O}(10^1)$  mm, significant bending or curvature can occur at this scale thus moving the fibres away from the desired relative scanning orientations. However, if the ROI is small, a minimal number of scans would still be sufficient as the target anatomy would be locally straight enough for MADI to work with the chosen scanning orientations. Deviations as much as 10° were allowed for when choosing scanning orientations, therefore allowing for some local bending/curvature before more scans are necessary.

Because the MADI technique will most likely be applied at low field, the robustness of the method at low SNR is important. Figs. 7–9 all show that the MADI technique remains accurate until an SNR of roughly 20. Furthermore, since the scanning orientations found in the present work attempt to capture the peak of the Magic Angle effect and



the domain relatively close to it, the signal in the region of interest will be boosted.

## 5. Conclusion

The main result presented here is that with a priori knowledge, 4 scanning orientations can be used to accurately estimate the collagen fibre orientations in target anatomy, such as the patella tendon using the MADI technique. The scanning orientations chosen should capture the peak and at least one point either side of it, with an additional scanning orientation to provide extra constraints on the estimated fibre directions. In the case of the patella tendon studied here, the main field should be oriented at 30°, 40°, 55°, 70°, relative to the tendon as found from the simulation studies. The simulation studies suggest there is  $\approx 10^\circ$  of tolerance which enabled the use of (mean) orientations of 29.0°, 34.5°, 56.5°, 68.8° relative to the patella which yielded accurate results in comparison to the gold standard reference data.

In practice, application of the technique in vivo would likely consist of a scout scan and then a set of 4 scans based on information from the scout. Even with fairly accurate a priori information, it is unlikely that  $B_0$  can be precisely oriented relative to the target anatomy. The lenient tolerances on the selection of scanning orientations therefore serves to counter this imprecision. The MADI technique itself has successfully been updated to use fully automatic soft registration which will aid with correction of geometric distortions in the images due to imaging at low field, gradient non-linearities, and soft body deformations. This is a large upgrade over our previous work as registration by manual adjustment is no longer necessary. The technique also shows robustness to low SNR, which will be unavoidable at the low field strength of our prototype scanner. Our scanner can yaw and rotate to capture the necessary images at the angles required for MADI.

In the present work the gold standard dataset was used to generate the segmentation label using standard deviation across the image set as a metric. The same segmentation label was used for all datasets/subsets in order to allow for direct voxel-voxel comparison between them. However, with only 4 scans the standard deviation metric is not as powerful. In lieu of using this metric, manual segmentation of the target anatomy could be performed on the ROI of the fixed image, which could then be applied to the registered images as well. Future work will also focus on other automatic segmentation techniques of the target anatomy such as applying the MADI technique to the whole ROI and then selectively pruning voxels unlikely to contain collagen based on fibre alignment metrics. Even though current segmentation metrics may suffer when using fewer scans, we have shown that fibre estimation accuracy is retained with as few as 4 scans hence allowing for detection of pathologies.

The scope of future work will cover application of MADI on our prototype scanner and detection and assessment of pathologies in samples and in vivo. Having shown that  $N = 4$  is sufficient to render fibre directions that are close to the assumed direction of the target anatomy, we predict that MADI with minimal scans will detect these regions by either rendering them correctly – if the fibres are within the scanning orientation tolerance – or the fibre directions will not converge in a damaged region. Either scenario would indicate a damaged or diseased region, however, this is something that will be explored as our work develops.

## CRediT authorship contribution statement

**Harry Lanz:** Conceptualization, Methodology, Software, Validation, Formal analysis, Investigation, Data curation, Writing – original draft, Writing – review & editing, Visualization. **Mihailo Ristic:** Conceptualization, Methodology, Resources, Writing – review & editing, Supervision, Project administration, Funding acquisition. **Karyn E. Chappell:** Methodology, Validation, Investigation, Resources, Data curation. **John V.M. McGinley:** Methodology.

## Declaration of competing interest

The authors declare that they have no known competing financial interests or personal relationships that could have appeared to influence the work reported in this paper.

## Data availability

Data will be made available on request.

## Acknowledgement

This work was partly supported by the Wellcome Trust Innovator Award WT215908/Z/19/Z.

## References

- [1] Devitt BM, O'Sullivan R, Feller JA, Lash N, Porter TJ, Webster KE, Whitehead TS. MRI is not reliable in diagnosing of concomitant anterolateral ligament and anterior cruciate ligament injuries of the knee. *Knee Surg Sports Traumatol Arthroscopy: Off J ESSKA* 2017;25(4):1345–51. <http://dx.doi.org/10.1007/s00167-017-4538-2>.
- [2] Temponi EF, de Carvalho Júnior LH, Sonnerly-Cottet B, Chambat P. Partial tearing of the anterior cruciate ligament: diagnosis and treatment. *Rev Bras Orthop (Engl Ed)* 2015;50(1):9–15. <http://dx.doi.org/10.1016/j.rboe.2015.02.003>.
- [3] Van Dyck P, Vanhoenacker FM, Gielen JL, Dossche L, Van Gestel J, Wouters K, Parizel PM. Three tesla magnetic resonance imaging of the anterior cruciate ligament of the knee: can we differentiate complete from partial tears? *Skelet Radiol* 2010;40(6):701–7. <http://dx.doi.org/10.1007/s00256-010-1044-8>.
- [4] Tjoumakaris FP, Donegan DJ, Sekiya JK. Partial tears of the anterior cruciate ligament: diagnosis and treatment. *Am J Orthop (Belle Mead NJ)* 2011;40(2):92–7.
- [5] Amin NH, Hussain W, Ryan J, Morrison S, Miniaci A, Jones MH. Changes within clinical practice after a randomized controlled trial of knee arthroscopy for osteoarthritis. *Orthop J Sports Med* 2017;5(4):2325967117698439. <http://dx.doi.org/10.1177/2325967117698439>.
- [6] Hamilton DF, Howie CR. Knee arthroscopy: influence of systems for delivering healthcare on procedure rates. *BMJ (Online)* 2015;351:h4720. <http://dx.doi.org/10.1136/bmj.h4720>.
- [7] Bydder M, Rahal A, Fullerton GD, Bydder GM. The magic angle effect: A source of artifact, determinant of image contrast, and technique for imaging. *J Magn Reson Imaging* 2007;25(2):290–300. <http://dx.doi.org/10.1002/jmri.20850>.
- [8] Szevenyi NM, Bydder GM. Dipolar anisotropy fiber imaging in a goat knee meniscus. *Magn Reson Med* 2011;65(2):463–70. <http://dx.doi.org/10.1002/mrm.22645>.
- [9] Seidel T, Hammer N, Garnov N, Schneider G, Steinke H. An algorithm for the calculation of three-dimensional collagen fiber orientation in ligaments using angle-sensitive MRI. *Magn Reson Med* 2013;69(6):1594–602. <http://dx.doi.org/10.1002/mrm.24408>.
- [10] Bruijic D, Chappell KE, Ristic M. Accuracy of collagen fibre estimation under noise using directional MR imaging. *Comput Med Imaging Graph* 2020;86:101796. <http://dx.doi.org/10.1016/j.compmedimag.2020.101796>.
- [11] Chappell KE, Bruijic D, Van Der Straeten C, Meeson R, Gedroyc W, McRobbie D, Ristic M. Detection of maturity and ligament injury using magic angle directional imaging. *Magn Reson Med* 2019;82(3):1041–54. <http://dx.doi.org/10.1002/mrm.27794>.
- [12] McGinley JV, Ristic M, Young IR. A permanent MRI magnet for magic angle imaging having its field parallel to the poles. *J Magn Reson* (1997) 2016;271:60–7. <http://dx.doi.org/10.1016/j.jmr.2016.08.001>.
- [13] Fullerton GD, Rahal A. Collagen structure: The molecular source of the tendon magic angle effect. *J Magn Reson Imaging* 2007;25(2):345–61. <http://dx.doi.org/10.1002/jmri.20808>.
- [14] de Oliveira A, Rauschenberg J, Beyersdorff D, Semmler W, Bock M. Automatic passive tracking of an endorectal prostate biopsy device using phase-only cross-correlation. *Magn Reson Med* 2008;59(5):1043–50. <http://dx.doi.org/10.1002/mrm.21430>.
- [15] Parker JR. *Algorithms for image processing and computer vision*. New York: Wiley; 1997.
- [16] Franco E, Bruijic D, Rea M, Gedroyc WM, Ristic M. Needle-guiding robot for laser ablation of liver tumors under MRI guidance. *IEEE/ASME Trans Mechatronics* 2016;21(2):931–44. <http://dx.doi.org/10.1109/TMECH.2015.2476556>.
- [17] Klein S, Staring M, Murphy K, Viergever M, Pluim J. elastix: A tool-box for intensity-based medical image registration. *IEEE Trans Med Imaging* 2010;29(1):196–205. <http://dx.doi.org/10.1109/TMI.2009.2035616>.
- [18] Rueckert D, Sonoda L, Hayes C, Hill D, Leach M, Hawkes D. Nonrigid registration using free-form deformations: application to breast MR images. *IEEE Trans Med Imaging* 1999;18(8):712–21. <http://dx.doi.org/10.1109/42.796284>.

- [19] Unser M. Splines: a perfect fit for signal and image processing. *IEEE Signal Process Mag* 1999;16(6):22–38. <http://dx.doi.org/10.1109/79.799930>.
- [20] Maes F, Collignon A, Vandermeulen D, Marchal G, Suetens P. Multimodality image registration by maximization of mutual information. *IEEE Trans Med Imaging* 1997;16(2):187–98. <http://dx.doi.org/10.1109/42.563664>.
- [21] Viola P, Wells WM. Alignment by maximization of mutual information. *Int J Comput Vis* 1997;24(2):137–54. <http://dx.doi.org/10.1023/A:1007958904918>.
- [22] Mattes D, Haynor D, Vesselle H, Lewellen T, Eubank W. PET-CT image registration in the chest using free-form deformations. *IEEE Trans Med Imaging* 2003;22(1):120–8. <http://dx.doi.org/10.1109/TMI.2003.809072>.
- [23] Thévenaz P, Unser M. Optimization of mutual information for multiresolution image registration. *IEEE Trans Image Process* 2000;9(12):2083–99. <http://dx.doi.org/10.1109/83.887976>.
- [24] Klein S, Pluim J, Staring M, Viergever M. Adaptive stochastic gradient descent optimisation for image registration. *Int J Comput Vis* 2009;81(3):227–39. <http://dx.doi.org/10.1007/s11263-008-0168-y>.
- [25] Ridgway G. Rice/rician distribution. 2008, <https://uk.mathworks.com/matlabcentral/fileexchange/14237-rice-rician-distribution>. [Online; accessed Dec 20, 2021].
- [26] Fedorov A, Beichel R, Kalpathy-Cramer J, Finet J, Fillion-Robin J-C, Pujol S, Bauer C, Jennings D, Fennessy F, Sonka M, Buatti J, Aylward S, Miller JV, Pieper S, Kikinis R. 3D slicer as an image computing platform for the quantitative imaging network. *Magn Reson Imaging* 2012;30(9):1323–41. <http://dx.doi.org/10.1016/j.mri.2012.05.001>.
- [27] Zhang F, Noh T, Juvekar P, Frisken SF, Rigolo L, Norton I, Kapur T, Pujol S, Wells W, Yarmarkovich A, Kindlmann G, Wassermann D, San Jose Estepar R, Rathi Y, Kikinis R, Johnson HJ, Westin C-F, Pieper S, Golby AJ, O'Donnell LJ. SlicerDMRI: Diffusion MRI and tractography research software for brain cancer surgery planning and visualization. *JCO Clin Cancer Inform* 2020;4(4):299–309. <http://dx.doi.org/10.1200/CCI.19.00141>.